Journal of Colloid and Interface Science 498 (2017) 449–459

Contents lists available at ScienceDirect

Journal of Colloid and Interface Science

journal homepage: www.elsevier.com/locate/jcis

Regular Article

Fine cutting edge shaped Bi_2O_3rods/reduced graphene oxide (RGO) composite for supercapacitor and visible-light photocatalytic applications

D. Maruthamani [a], S. Vadivel [a,*], M. Kumaravel [a], B. Saravanakumar [b], Bappi Paul [c], Siddhartha Sankar Dhar [c], Aziz Habibi-Yangjeh [d], A. Manikandan [e], Govindarajan Ramadoss [f]

[a] *Department of Chemistry, PSG College of Technology, Coimbatore 641004, India*
[b] *Department of Physics, Dr. Mahalingam College of Engineering and Technology, Pollachi 642003, Tamil Nadu, India*
[c] *Department of Chemistry, National Institute of Technology, Silchar 788010, Assam, India*
[d] *Department of Chemistry, Faculty of Science, University of Mohaghegh Ardabili, PO Box 179, Ardabil, Iran*
[e] *Department of Chemistry, Bharath Institute of Higher Education and Research, Bharath University, Chennai 600 073, Tamil Nadu, India*
[f] *PSG Institute of Advanced Studies, Coimbatore 641004, India*

GRAPHICAL ABSTRACT

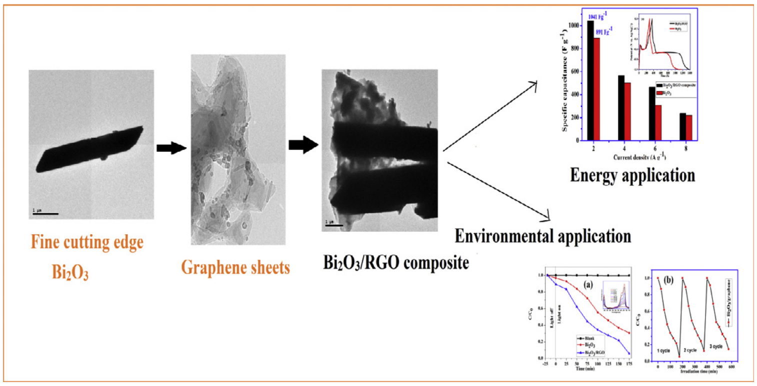

ARTICLE INFO

Article history:
Received 27 December 2016
Revised 18 February 2017
Accepted 21 March 2017
Available online 22 March 2017

Keywords:
Bi_2O_3 rods
Graphene
Calcination
Supercapacitor
Photocatalyst

ABSTRACT

Bi_2O_3 rods/RGO composite has been synthesized by a simple precipitation and calcination method. The crystallnity, structural, and morphological features were studied by X-ray diffraction (XRD), field-emission scanning electron microscopy (FE-SEM), and high resolution transmission electron microscopy (HR-TEM) techniques. The supercapacitor behavior was studied using cyclic voltammetry, galvanostatic charge discharge and impedance analysis, respectively. The Bi_2O_3 rods/RGO nanocomposite exhibits a maximum specific capacitance of 1041 F g^{-1} at a current density of 2 A g^{-1}. The photocatalytic activity of Bi_2O_3 rods/RGO composite was evaluated by photocatalytic degradation of methylene blue (MB) dye under visible-light irradiation. The enhancement of photocatalytic properties of Bi_2O_3 rods/RGO composite attributed to the synergistic effect between Bi_2O_3 rods and graphene sheets which effectively prevents recombination of the photogenerated electron-hole pairs in Bi_2O_3 rods. The present study provides a new approach in improving the performance of Bi_2O_3 rods/RGO composite in energy and environmental applications.

---

* Corresponding author.
E-mail address: vlvelu7@gmail.com (S. Vadivel).

http://dx.doi.org/10.1016/j.jcis.2017.03.086
0021-9797/

1. Introduction

Electrochemical capacitors or supercapacitors are supposed to be a kind of promising candidate for energy storage devices owing to their high power density and long cycle life [1–3]. There are two types of supercapacitors in practice namely, electrochemical double layer capacitors (EDLCs) and pseudocapacitors. In EDLCs, the energy is stored electrostatically at the electrode-electrolyte interface of the double layer, while in pseudocapacitors, charge storage occurs by redox reactions on the electrode surface [4,5]. Therefore, the capacitive performance of supercapacitor mainly depends upon the physical and chemical properties of the electrode materials. Metal oxides like RuO_2 [6], NiO [7], MnO_2 [8], Bi_2O_3 [9], and conducting polymers [10,11] are conventional pseudocapacitive materials. Thus, the pseudocapacitor materials hold the potential for the next generation of supercapacitor electrodes [12]. The main drawbacks of pseudocapacitive electrodes are poor conductivity, sluggish redox reaction, and intrinsic structural degradation during the charging-discharging process [13]. To overcome this problem, much efforts have been devoted to combine pseudocapacitor electrode with carbonaceous materials solve these issues [14]. However, the previous reports clearly indicated that the incorporation of carbon materials on pseudocapacitor materials can dramatically improves the specific surface area [15].

On the other hand, photocatalysis is an advanced oxidation process, which showed a good performance in degradation of organic pollutants [16]. The environmental pollutants can be effectively degraded with the presence of active species like hydroxyl and superoxide radicals, which are generated by heterogeneous photocatalysts under an appropriate light irradiation [17]. Compared with other usual treatment methods, photocatalytic processes exhibited the salient features of non-toxicity and excellent stability for consequent cycle usage [18]. Many works showed that bismuth based materials like Bi_2WO_6 [19], $BiVO_4$ [20], Bi_2O_3 [21], and Bi_2S_3 [22] have good visible-light photocatalytic activity and superior electrochemical properties.

Among them, bismuth oxide (Bi_2O_3) is a promising semiconductor material for environmental and energy applications, due to its excellent photocatalytic performance, refractive index, and photoluminescence properties [23]. These unique properties have made as suitable for the important applications such as gas sensors [24], fuel cells [25], optical coatings [26], supercapacitors [27], photocatalysts [28], and photovoltaic devices [29]. To date, many Bi_2O_3 nanostructures have been successfully synthesized, including rods, belts, flakes, particles, and thin films [30].

The application of Bi_2O_3 in supercapacitors was first reported by Gujar et al. [31]. The Bi_2O_3 films were prepared by electrodeposition method and exhibited specific capacitance of 98 F g^{-1}. Yuan et al. [32] reported bismuth oxide/worm-like carbon composite using microwave approach and exhibited maximum specific capacitance of 386 F g^{-1}. Huang et al. [33] prepared rod-like Bi_2O_3 by sol-gel method and demonstrated specific capacitance of 528 F g^{-1} at the scan rate of 5 mV s^{-1}. Wang et al. [34] synthesized Bi_2O_3/graphene by a solvothermal approach and the specific capacitance of 255 F g^{-1} was obtained at a current density of 1 A g^{-1}. It is important to note that the synthesis of Bi_2O_3 incorporated carbon composites materials could enhance the electrochemical properties.

To further improve the visible-light photocatalytic activity of Bi_2O_3, many studies have been done. Graphene is one of the most studied versatile material to combine with Bi_2O_3, owing to its large surface area, high electronic conductivity and excellent electrochemical properties [35]. In addition, graphene was exploited as one of the most promising candidates for supercapacitor electrodes which provide long cycle life for supercapacitors [36]. Both the excellent electronic conductivity of graphene and the pseudocapacitive nature of Bi_2O_3, they can work together to gain the higher specific capacitance and long cycle stability in supercapacitors [37].

Herein, we report a simple and cost effective technique for the synthesis of Bi_2O_3 rods/RGO composite using simple precipitation and calcination method. This hybrid material exhibited higher specific capacitance and better cyclic stability. Furthermore, the photocatalytic properties of the Bi_2O_3 and Bi_2O_3 rods/RGO composite was evaluated through the degradation of MB dye under visible-light irradiation. Finally, a possible mechanism for enhanced photocatalytic activity and electrochemical properties was proposed.

2. Experimental

2.1. Materials

All chemicals used in this present study were of analytical grade and used without any further purification. Bismuth nitrate pentahydrate ($Bi(NO_3)_3{\cdot}5H_2O$), potassium hydroxide, polyethylene glycol 6000 (PEG), potassium permanganate, sodium nitrate, hydrogen peroxide (30%), and sulphuric acid (98%) were obtained from SRL Chemicals private, Ltd. India. Graphite powder was obtained from Loba Chemicals, India.

2.2. Synthesis of Bi_2O_3 rods/RGO composite

Graphene oxide (GO) was prepared according to our previous reported literature [38]. The Bi_2O_3 rods/RGO nanocomposite was prepared as follows. First, 0.45 g of ($Bi(NO_3)_3{\cdot}5H_2O$) and 0.015 g of GO was dissolved in 50 ml of dilute nitric acid (0.1 M) and it was placed in an ultrasonic bath and irradiated for 30 min to form a homogenous suspension at temperature of about 25 °C. Then, 0.25 g of KOH was added to the above solution and irradiated for another 10 min at the same temperature to get a pale yellow suspension. Then, the prepared sample was separated and dried in oven at a temperature of 60 °C for 8 h. Finally, the product was subject to calcination with a heating rate of 5 °C/min for 4 h at 500 °C. The pure Bi_2O_3 rods were also prepared by the similar procedure except for the addition of GO sheets.

2.3. Characterization techniques

Powder X-ray diffraction (XRD) study was performed with Xpert-Pro-PAN analytical instrument with Cu-Kα radiation (45 kV, 30 mA, $\lambda = 0.15418$ nm) between the 2 theta values of 10 and 70°. Field-emission scanning electron microscopy (FESEM, Hitachi S-4800, Japan), transmission electron microscopy (Hitachi H7650 electron microscope), and energy-dispersive X-ray spectroscopy (EDS) were used to characterize surface morphology and chemical compositions of the Bi_2O_3 rods/RGO nanocomposite. Raman spectra were recorded using Nanophoton confocal Raman micro spectrophotometer at visible light range of 532 nm. Fourier transform infrared (FT-IR) spectrum was analyzed using PERKIN ELMER RX-1 FT-IR spectrophotometer. UV–vis diffused reflectance spectra (UV–vis DRS) of Bi_2O_3 and Bi_2O_3 rods/RGO nanocomposite were obtained using UV-2450 (Shimadzu) UV–vis spectrophotometer. Electrochemical and photocurrent studies were carried out by CHI660D electrochemical workstation.

2.4. Electrochemical measurements

The working electrodes for super capacitor studies were prepared as follows. Briefly, the graphite sheet electrode (1×1 cm^2)

washed with acetone and dried at 65 °C under vacuum. The active material (80 wt%), acetylene black (10 wt%), and PTFE (10 wt%) were mixed uniformly to form a homogenous slurry using ethanol as the solvent. Then, the slurry was coated onto the pretreated graphite sheet electrode and dried at 70 °C. Electrochemical studies were carried out in a 6M potassium hydroxide (KOH) electrolyte at room temperature. A platinum wire was used as the counter electrode and Ag/AgCl was used as the reference electrode. The active material mass of the electrode was about 2 mg. Cyclic voltammetry (CV) studies were carried out in the potential window range of -1.0 to 0.0 V at different scan rates (2–40 mV s^{-1}). The galvanostatic charge-discharge (GCD) studies were performed at various current densities (2–8 A g^{-1}) over a potential window from −1.0 to 0.0 V. Electrochemical impedance spectroscopy (EIS) studies was recorded in a frequency range from 0.01 Hz to10 kHz.

2.5. Photo-electrochemical studies

In a typical working electrode preparation, 3 mg of the catalyst was ground with 5 mL of polyethylene glycol and 10 mL of deionized water to make homogeneous slurry. The slurry was coated with conducting side of the FTO glass plate by doctor blade method. Then, it was dried in hot air oven. The 0.1 M Na_2SO_4 was used as electrolyte and 100 W halogen lamps were used as the visible-light source. The photoelectrochemical properties were investigated with a electrochemical workstation in a conventional three electrode system with a Pt-wire as a counter electrode, Ag/AgCl (in saturated KCl) as a reference electrode and active material coated FTO glass plate as a working electrode respectively.

2.6. Evaluation of photocatalytic activity

The photocatalytic activities of the synthesized materials were evaluated through the degradation of MB dye under visible-light irradiation. A 300 W xenon lamp was used as the visible-light source and the irradiation time was optimized as 175 min. The temperature of the reactor was adjusted by a water bath circulation system. In all experiments, the as-synthesized photocatalysts (0.1 g) were added to 100 mL aqueous solution of MB (10 mg/L) aqueous solution without any pH adjustment. The suspension was ultrasonicated for 2 min and stirred at a speed of 500 rpm for 20 min in the dark condition before the irradiation, in order to achieve an adsorption-desorption equilibrium between the MB dye and the photocatalyst. During each photocatalytic experiment, 2 mL of the aliquot was collected and the concentration of MB was evaluated using a UV–vis spectrophotometer by measuring the maximum absorbance wavelength at 663 nm.

3. Results and discussion

3.1. XRD analysis

The crystal structure and purity of the synthesized Bi_2O_3 and Bi_2O_3 rods/RGO composite were determined by XRD analysis. Fig. 1 shows the XRD patterns of GO, Bi_2O_3 and Bi_2O_3 rods/RGO composite, respectively. The XRD pattern of the pure GO shows a prominent peak at (2θ = 10.7°) corresponding to the (002) reflection of the GO, viewing that complete oxidation of graphite into the graphene oxide. The XRD patterns of Bi_2O_3 and Bi_2O_3/RGO composite confirms that the Bi_2O_3 exhibits monoclinic phase with space group of P21/c. The diffraction peaks present in the XRD was well-indexed with JCPDS card no: 41-1449. No other diffraction peaks related with any impurities were detected in the XRD spectrum of both Bi_2O_3 and Bi_2O_3 rods/RGO composite, which further confirms that the prepared materials are in the pure form [39]. Moreover, no obvious peak of RGO can be observed, that might attribute to the high crystallanity of Bi_2O_3 and lesser weight percentage of RGO in the nanocomposite [40].

3.2. FT-IR spectroscopy

FT-IR spectroscopy was used to identify the chemical bonding in the GO, RGO, Bi_2O_3 and Bi_2O_3/RGO composite, as shown in Fig.2. In the spectrum of pure GO, the broad peak around the 3355 cm^{-1}can be attributed to the O—H stretching vibration. The strong absorption bands at the 1733 $cm^{-1}$and 1630 $cm^{-1}$are attributed to the C=O and C=C stretching vibrations, respectively [35,36]. The peaks around 1403 cm^{-1} is corresponding to the stretching vibrations of C—O respectively. FTIR spectrum of the pure Bi_2O_3 shows major absorption peaks at 847 cm^{-1}, 1363 cm^{-1}, 1648 cm^{-1} respectively. The peak at 847 cm^{-1} is due to the symmetrical stretching vibration of the Bi—O—Bi group of the BiO_3 pyramidal unit. The peak at 1092 cm^{-1} is ascribed to O—O stretching mode. The absorption at 1363 cm^{-1} is due to stretching vibration of Bi—O bond. Furthermore, the peak at 1650 cm^{-1} is assigned to surface carbonate species [9,21]. The main characteristic peaks of Bi—O—Bi and Bi—O stretching vibration in pure Bi_2O_3 show slight shift to lower wave number in Bi_2O_3/RGO composite. This shift confirms the formation of close interaction between the Bi_2O_3 and RGO counterparts of the composite.

3.3. Raman spectroscopy

The Raman spectra of GO and Bi_2O_3/RGO composite are presented in Fig.3. The Raman spectrum of GO shows two prominent peaks at 1345 cm^{-1}(D band) and 1575 cm^{-1} (G band). The D band is a common feature for sp^3 defects in carbon, and the G band provides an information about in-plane vibration of sp^2-bonded carbon atoms in a two dimensional hexagonal lattice. The broadening of the D and G bands is due to the introduction of oxygen functional groups during the oxidation process such as hydroxyls and epoxides. The Raman spectrum of Bi_2O_3 rods/RGO composite shows remarkable shifts and the D and G bands appear at 1339 and 1590 cm^{-1}, respectively [35]. Compared to the pure GO, the Bi_2O_3 rods/RGO composite shows an increment in I_D/I_G ratio (0.98–1.05) [36]. The increased I_D/I_G ratio in the Bi_2O_3 rods/RGO composite suggests that a decrease in the size of sp^2 domains upon the removal of oxygen functional groups in GO [37].

3.4. Morphological studies

FE-SEM images of the Bi_2O_3 and Bi_2O_3 rods/RGO composite were shown in Fig. 4(a–d). Fig. 4a and b shows the FE-SEM image of the Bi_2O_3, which revealed that the as-synthesized Bi_2O_3 possess a unique rod-shape structure which are grown with high density. The diameters of the rods are in the range of 1–1.5 μm while the average lengths are in the range of 2-4 μm respectively. Fig.4(c and d) shows the typical FE-SEM image of Bi_2O_3 rods/RGO composite, which shows that the RGO sheets wrapped tightly on the surface of the Bi_2O_3 rods. Thus, the flexible and good conductive nature of RGO could provide excellent conducting pathway for this composite as good photocatalyst and supercapacitor [41].

Fig. 5(a–d) exhibits the HR-TEM images of the prepared Bi_2O_3 and Bi_2O_3 rods/RGO composite. The HR-TEM images are in full consistent with FE-SEM results in terms of morphology as well as dimensionality. Fig. 5(a and b) shows typical HR-TEM images for a single micro-rod, which revealed that the synthesized nanorods possessing smooth as well and clean surface with ultra fine cutting edges. The HR-TEM image (Fig. 5c) taken from the edge of the Bi_2O_3 rods reveals that the lattice fringe of about

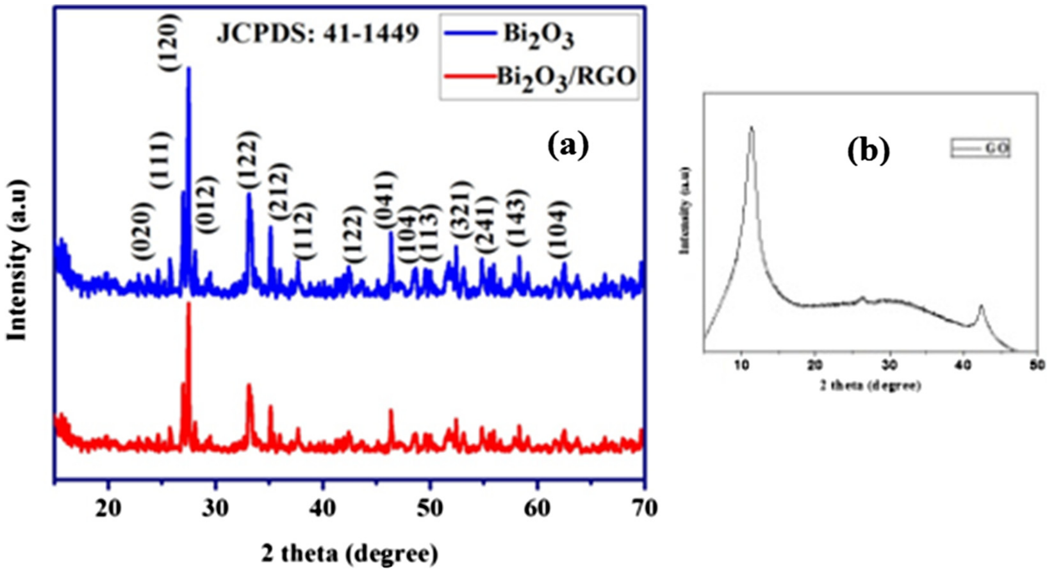

Fig. 1. XRD patterns of the Bi_2O_3 and Bi_2O_3 rods/RGO composite.

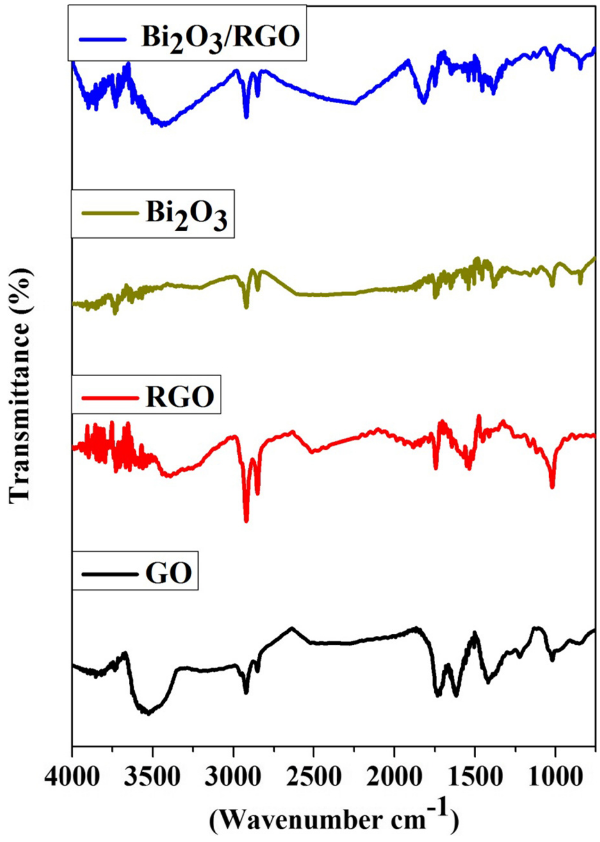

Fig. 2. FT-IR spectra of the GO, RGO, Bi_2O_3, and Bi_2O_3 rods/RGO composite.

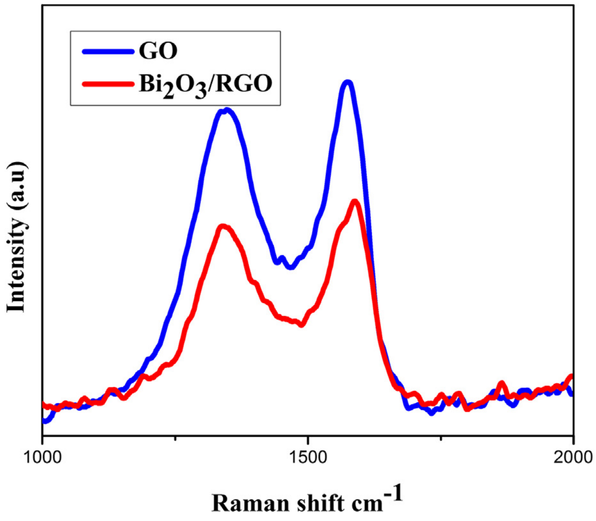

Fig. 3. Raman spectra of the GO and Bi_2O_3 rods/RGO composite.

0.330 nm, corresponding to the (1 2 0) plane of monoclinic phase of Bi_2O_3, which is consistent with the XRD results [42]. Fig. 5d shows the uniform deposition of Bi_2O_3 micro-rods in RGO sheets which confirm the successful preparation of Bi_2O_3 rods/RGO composite.

3.5. EDS elemental mapping analysis

EDS mappings were performed to investigate the elemental distribution and purity of the Bi_2O_3 rods/RGO composite and the results are shown in Fig. 6(a–d). The EDS mapping of the elements indicate that the Bi_2O_3 has homogeneously deposited over the RGO sheets, which supports the corresponding FE-SEM results. Additionally, the existence of Bi, C, and O in the nanocomposite has been proved by the representative peaks in the EDS data (Fig. 6a). Thus, Bi and O elements originated from the Bi_2O_3, and the C peak arises from the RGO counterparts of the composite (Fig. 6b–d).

3.6. Electrochemical studies

To explore the energy storage behavior of the Bi_2O_3 rods/RGO composite, cyclic voltammetry (CV) and galvanostatic charge discharge (GCD) studies were carried out in 6 M KOH electrolyte. Fig. 7a shows CV curves of the Bi_2O_3 and Bi_2O_3 rods/RGO composite between the potential window of −1.0 to 0 V at a scan rate of 2 mV s^{-1}. A pair of redox peaks is observed for the Bi_2O_3 electrode confirming the significant influence of pseudocapacitive nature [43]. The redox peaks at −0.53 and 0.79 V for the Bi_2O_3 could be attributed to the reversible redox reactions of Bi^{3+} to metallic Bi

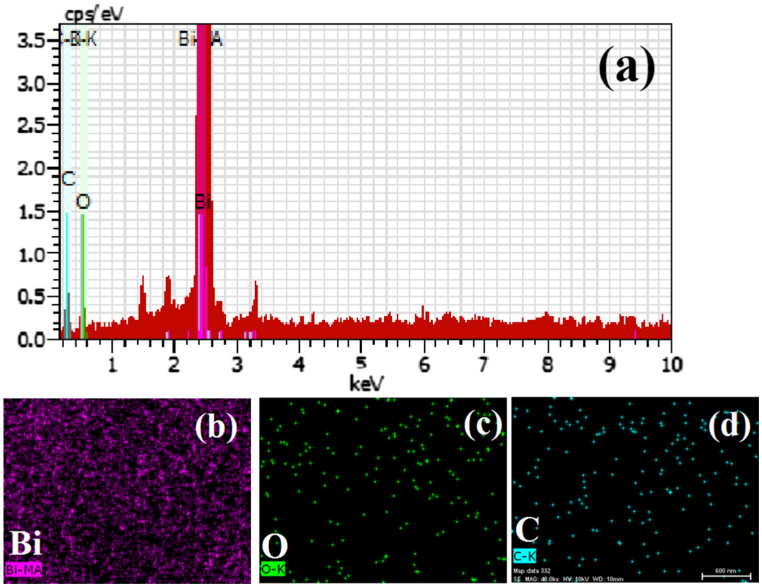

Fig. 6. EDS mapping analysis of the Bi_2O_3 rods/RGO composite.

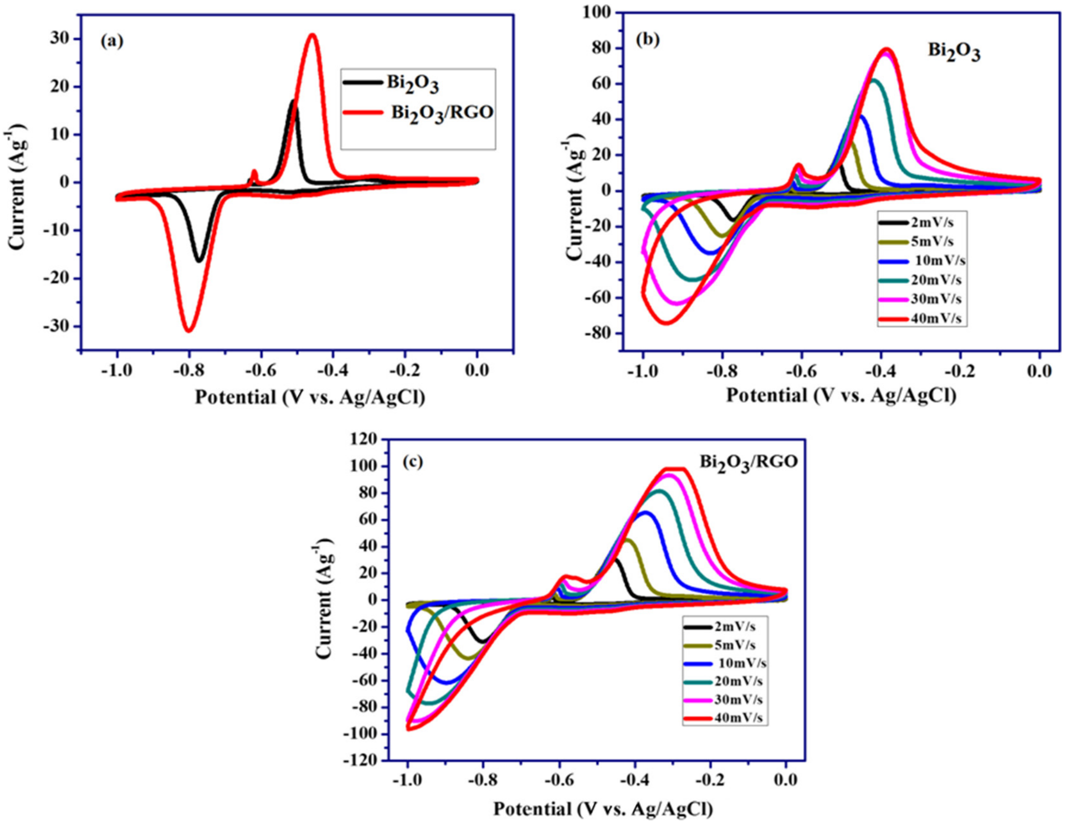

Fig. 7. (a) CV curves of the Bi_2O_3 and Bi_2O_3 rods/RGO composite compared at 2 mV/s; (b) CV curves of the Bi_2O_3 and Bi_2O_3 rods/RGO composite recorded at various scan rates.

[44]. The small peak around −0.6 V is due to the catalytic induction or the oxidation of some untransformed Bi^0 during the process. The CV curves of the Bi_2O_3 rods/RGO composite and the pure Bi_2O_3 are fairly similar in shape. Moreover, it is observed that the onset potential of the oxidation and reduction peaks of the Bi_2O_3/RGO shifts slightly compared to that of the pure Bi_2O_3. The peak current of the redox couple for the Bi_2O_3 rods/RGO composite are higher than those of the bare Bi_2O_3. Obviously, the CV curves of the Bi_2O_3 rods/RGO composite display larger integrated area than the Bi_2O_3 at the same scan rate, revealing the higher energy storage capacity of the electrode material [45]. The CV curves of Bi_2O_3 and Bi_2O_3 rods/RGO composite electrodes at various scan rates (2–40 mV s^{-1}) are demonstrated in (Fig. 7b and c). As the scan rate increases, the cathodic peak position shifts to a lower potential and the anodic peak position shifts to a higher potential, which is attributed to the polarization effect of the electrode [46].

Galvanostatic charge-discharge (GCD) is a reliable method to estimate the specific capacitance of the supercapcitor electrode materials. GCD curves of the as synthesized Bi_2O_3 and Bi_2O_3/RGO nanocomposite at different current densities (2–8 A g^{-1}) between the potential window of −1.0 to 0 V are shown in Fig. 8(a and b). As consistent with the CV studies, the non linear behavior of charge-discharge curves at various current densities further confirms the pseudocapacitance nature of the Bi_2O_3/RGO nanocomposite [47]. It can be clearly observed that the very long discharge time of Bi_2O_3 rods/RGO composite compared with the pure Bi_2O_3 reveals that it has superior charge storage capacity than the pure Bi_2O_3. The specific capacitance values were calculated from the GCD curves by using the following equation [48]

$$SC = \frac{I \times \Delta t}{\Delta V \times m}\ \mathrm{F\,g^{-1}} \qquad (1)$$

where I (A) is the discharged current, Δt (s) is the discharge time, ΔV (V) represents the potential drop, and m (g) is the mass of the active material [49].

The specific capacitance of Bi_2O_3 rods/RGO composite electrode are calculated to be 1041, 568, 465, and 236 F g^{-1} at current densities of 2, 4, 6, and 8 A g^{-1}, respectively, which are much higher than that of the pure Bi_2O_3 electrode at the same current densities (891, 500, 306, and 230 F g^{-1}). The calculated specific capacitance as a function of current density is shown in Fig. 9. At lower current densities, the electrolyte ions have enough time to access interior parts of the electrode active material leading to the higher specific capacitance [50]. Furthermore, the electrode active material exhibits lower specific capacitance values at higher current densities due to the electrolyte ions does not have sufficient time to intercalate the active material completely [51].

Table 1 summarizes the capacitive performance of previously reported bismuth based electrode materials in terms of specific capacitance. The calculated specific capacitance of 1041 F g^{-1} obtained from the charge–discharge curve of the Bi_2O_3 rods/RGO composite material was quite higher than the previously reported composite electrode materials.

3.6.1. Electrolyte effect

In order to study about the effect of electrolyte in supercapacitor performance, the cyclic voltammetric studies and galvanostatic charge-discharge studies were also performed in 1 M NaCl solution to investigate the supercapacitor of the Bi_2O_3, Bi_2O_3 rods/RGO composite in deoxygenated electrolyte (Fig. S1a–d). As can be seen, the CV curves are closely resembles to KOH electrolyte, which indicates the capacitance mainly resulted by pseudo-capacitance. The redox behavior in terms of peak of the Bi_2O_3 in NaCl solution is quite differing from the behavior of alkaline solution (KOH) and it is based on the intercalation of sodium ions into the crystalline structure of the Bi_2O_3 [43]. The GCD studies confirms that the specific capacitance greatly decreases as 6 M KOH (1041 F g^{-1}) > 1 M NaCl (300 F g^{-1}). Therefore, higher the concentration of OH^- ion facilitates the redox reaction of $Bi_2O_3$and lead to more stored charge at electrode surface.

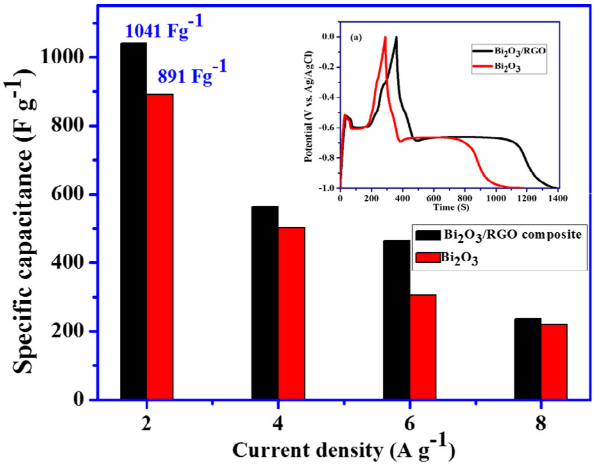

Fig. 9. Variation of specific capacitance of the pure Bi_2O_3 and Bi_2O_3 rods/RGO composite as a function of current density (Inset of figure) galvanostatic charge-discharge curves of the pure Bi_2O_3 and Bi_2O_3 rods/RGO composite electrodes at 2 Ag^{-1}.

The resistive behavior of the pristine Bi_2O_3 and Bi_2O_3 rods/RGO composite electrodes were analyzed using electrochemical impedance spectroscopy (EIS) measurements. The representative Nyquist plots of the Bi_2O_3 and Bi_2O_3 rods/RGO composite are presented in Fig. 10. In addition, the enlarge view of the same plot is presented in the inset of this figure. The Nyquist plot shows a semicircle in the high-frequency region and a straight line in the low-frequency region. The semicircle at the high-frequency region implies the charge transfer resistance value (R_{ct}), and the straight line in the low-frequency region implies the diffusive resistance [52]. Thus, the Bi_2O_3 rods/RGO composite electrode exhibits a smaller radius of semicircle in the high frequency region and a larger slope line in the low-frequency region compared with the pure Bi_2O_3 electrode, confirming that the fast charge transfer and ion diffusion processes happened at electrode material [53]. The R_{ct} values observed for the Bi_2O_3 and Bi_2O_3 rods/RGO composite are 1.3 and 10.9 Ω, respectively. It is noted that the R_{ct} value of Bi_2O_3

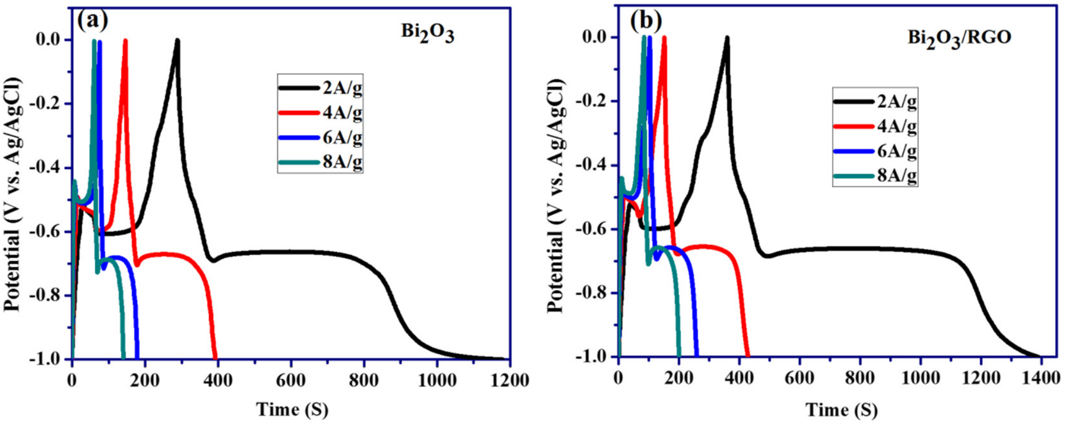

Fig. 8. Galvanostatic charge-discharge curves of (a) pure Bi_2O_3 and (b) Bi_2O_3 rods/RGO composite at different current densities.

Table 1
Summary of electrochemical performance of bismuth based electrode materials.

S. No	Electrode material	Electrolyte	Specific capacitance	Reference
1	Bi_2O_3 rods	6M KOH	528 Fg^{-1}	[9]
2	Bi_2O_3/activated carbon	1M Li_2SO_4	99.5 Fg^{-1}	[65]
3	Bi_2O_3 @MnO_2	1M Na_2SO_4	139.4 Fg^{-1}	[66]
4	Bi_2O_3/carbon	6M KOH	235 Fg^{-1}	[32]
5	Bi_2O_3 film	1M NaOH	98 Fg^{-1}	[31]
6	Bi_2O_3 rods/graphene	6M KOH	1041 Fg^{-1}	This work
7	Bi_2S_3/graphene	2M KOH	290 Fg^{-1}	[38]

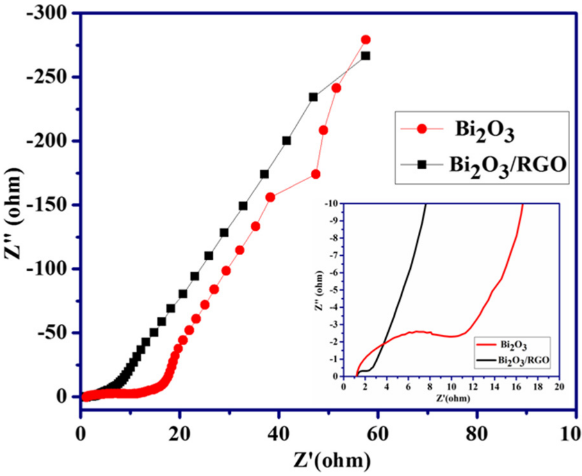

Fig. 10. Electrochemical impedance spectroscopy (EIS) plots of the pure Bi_2O_3 and Bi_2O_3 rods/RGO composite.

rods/RGO composite is lower than that of the bare Bi_2O_3. The lower charge transfer resistance for the composite electrode confirms the usefulness of adding RGO to the bare Bi_2O_3. Here RGO acts as conductivity booster and lowered the R_{ct} value of composite material. Due to lower value of R_{ct}, the Bi_2O_3 rods/RGO composite shows good electrochemical performance.

The cyclic stability is another important factor for commercial exploitation of electrode material. The cycle life test was carried out for over 1000 cycles at 2 A g^{-1} for the both prepared electrodes. Fig. 11 displays that the specific capacitance of the Bi_2O_3 rods/RGO composite electrode increases gradually and reaches the highest value after 100 cycles, and thereafter slightly decreases, which mainly due to activation of the electro active materials [54]. The specific capacitance retention for the Bi_2O_3/RGO nanocomposite electrode is about 94% after 1000 cycles, which is much better than 80% capacitance retention for the Bi_2O_3 electrode after the same cycles. This specific capacitance loss after several cycles is due to, the volume distortion of electrode materials caused by swelling or shrinkage during the reversible redox process [55]. However, in the Bi_2O_3 rods/RGO composite, graphene plays a crucial role in preventing the volume distortion of Bi_2O_3 counterpart during the redox process, subsequently improving the cyclic stability [56]. It is observed that this higher electrochemical performance of the prepared Bi_2O_3 rods/RGO composite could be attributed to the following reasons: (i) the in situ synthesis of the Bi_2O_3 rods/RGO composite provide effective interfacial contact between Bi_2O_3 rods and RGO nanosheets. (ii) The well-dispersed RGO with a high surface area in the composite provides a high conducting pathway, resulting in fast electron transfer and ion transport during the charging and discharging process [57].

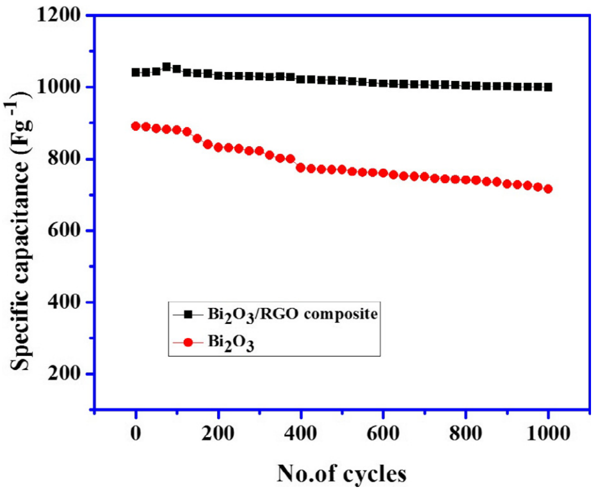

Fig. 11. Cyclic stability of the Bi_2O_3 rods/RGO composite at 2 Ag^{-1} upto 1000 cycles.

3.7. UV–vis DRS analysis

The UV–vis DRS spectra of the prepared Bi_2O_3 and Bi_2O_3 rods/RGO composite were recorded in the range of 200–900 nm. As shown in Fig. 12a, it can be obviously seen that Bi_2O_3 has a clear absorption edge around 464 nm in the visible-light region [58]. Compared with the spectrum of Bi_2O_3, the absorption edge of the Bi_2O_3 rods/RGO composite shows a slightly shift in to the higher wavelength (482 nm). A plot of the transformed Kubelka-Munk function of light energy $(\alpha hv)^2$ vs. energy (hv) is also shown in Fig. 12b. The band gaps of as-prepared photocatalysts are calculated as 2.82 and 2.75 eV respectively for the Bi_2O_3, and Bi_2O_3 rods/RGO composite [59]. This enhanced visible-light absorption ability of the nanocomposite will increase the degradation rate of MB dye.

3.8. Photocurrent studies

In order to confirm the photo-induced charge separation efficiency of the as-prepared Bi_2O_3, and Bi_2O_3 rods/RGO composite, the photocurrent studies were carried out and the results are shown in Fig. 13. Upon illumination, the photocurrent values increases sharply reaching a steady state and the current intensity returns quickly to the normal state when the light is turned off [60]. The presence of RGO leads to the enhancement of transient photocurrent response in Bi_2O_3 rods/RGO composite. Moreover, the transient photocurrent is fast, steady and reproducible during the consecutive cycles. Photocurrent results shows that addition of RGO to the Bi_2O_3 matrix reduces effectively the recombination rate of electron-hole pairs [61].

3.9. Photocatalytic degradation experiments

Fig. 14 shows the photocatalytic degradation profiles of MB over the Bi_2O_3 and Bi_2O_3 rods/RGO composite photocatalysts. It can be

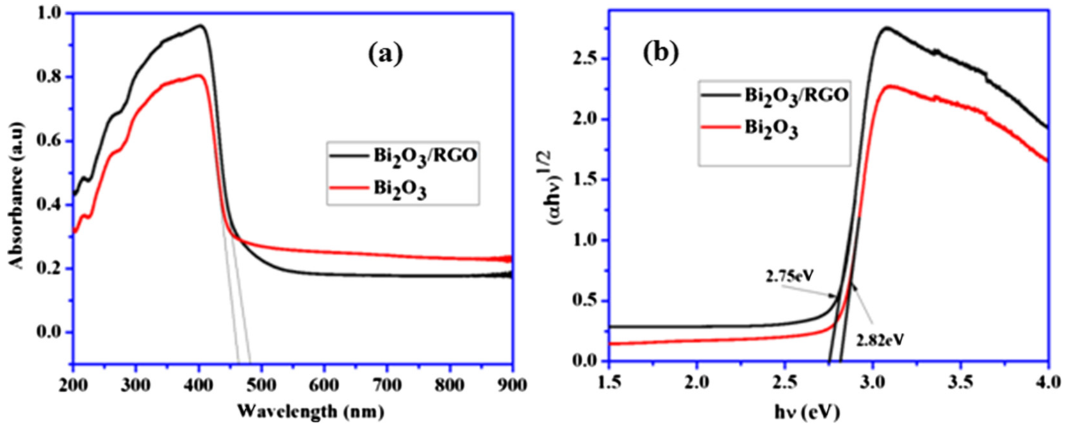

Fig. 12. UV–vis DRS spectra of the pure Bi_2O_3 and Bi_2O_3 rods/RGO composite.

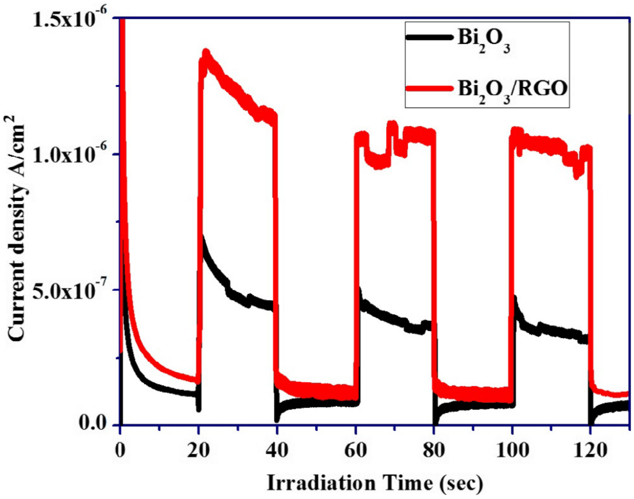

Fig. 13. Photocurrent studies of the pure Bi_2O_3 and Bi_2O_3 rods/RGO composite.

seen that MB shows mild degradation in the absence of any photocatalyst, reflecting high stability of MB molecules under the visible-light irradiation. It should be noted that the Bi_2O_3 rods/RGO composite exhibits increased adsorption ability for MB molecules than the pure Bi_2O_3. The higher adsorption capacity of MB dye over the surface of Bi_2O_3 rods/RGO composite can be beneficial for the improvement of photocatalytic degradation. However, obvious degradation of MB was observed in the presence of Bi_2O_3, where nearly 67% of the MB dye was degraded. It can be seen that the photocatalytic activity of Bi_2O_3 was dramatically improved after the modification with RGO. Thus, the Bi_2O_3 rods/RGO composite shows the highest photocatalytic activity (96%) which is quite higher than that of the pure Bi_2O_3 (Fig. 14a). The positive effect of RGO on the photocatalytic activity of the Bi_2O_3 sample can be ascribed to the strong interaction between Bi_2O_3 and highly conductive RGO sheets which facilitate the separation of electron-hole pairs [62]. The capability of reuse is one of the most serious issues for an ideal photocatalyst. Hence, the reusability and stability of the Bi_2O_3 rods/RGO composite was investigated [63]. The sample was collected after each degradation experiment and reused for three times. Fig. 14b shows the results of three successive MB degradation runs under the same experimental conditions. It can be seen that the Bi_2O_3 rods/RGO composite exhibits only 12% loss of its activity, which confirms the stability of the photocatalyst for degradation of MB pollutant [64]. Furthermore, the crystalline nature and structural stability of Bi_2O_3 rods/RGO composite was maintained even after the degradation of MB. Fig. 15 shows the XRD patterns of Bi_2O_3 rods/RGO composite which represents an unchanged crystalline structure, even after performing the photocatalytic experiments for three times, further implying the excellent stability and no phase transformation during the visible-light illumination [28,29]. Fig.16 depicts that the degradation rate constant (k value) of MB over the RGO, Bi_2O_3 and Bi_2O_3 rods/RGO composite samples are 0.0021, 0.0075, and 0.0132 min^{-1}, respectively. Hence, photocatalytic activity of the Bi_2O_3 rods/RGO

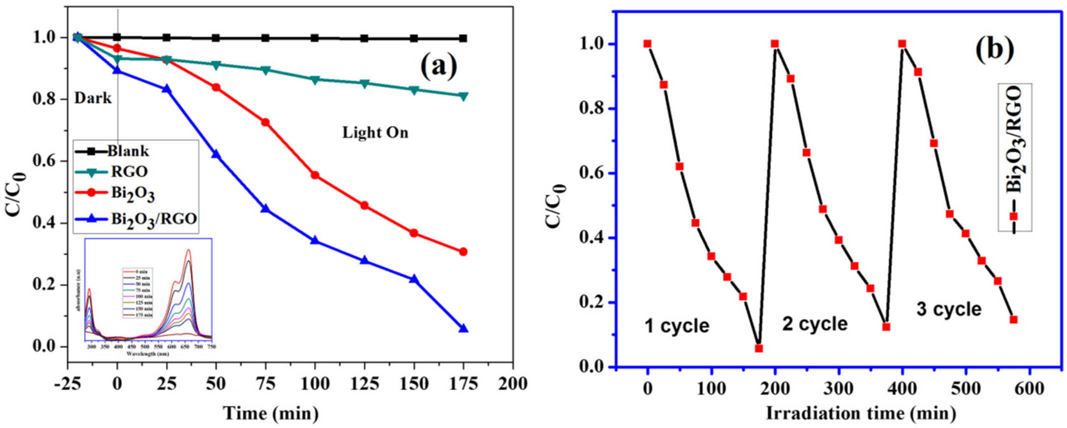

Fig. 14. (a) Plots of C/C_0 versus the irradiation time; (b) cyclic stability of the Bi_2O_3 rods/RGO composite towards MB degradation under visible-light irradiation.

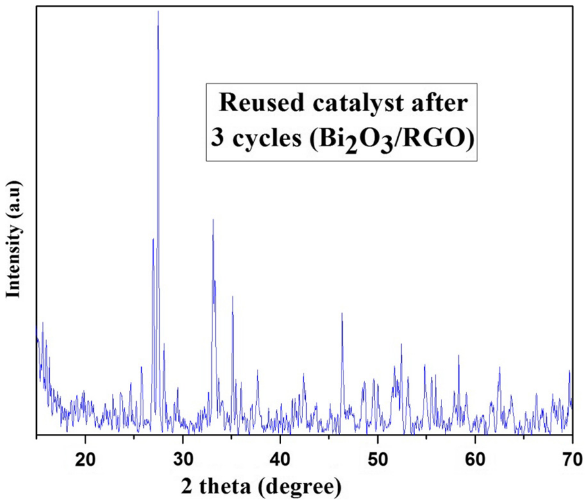

Fig. 15. XRD patterns of the Bi_2O_3 rods/RGO composite after three cycle tests.

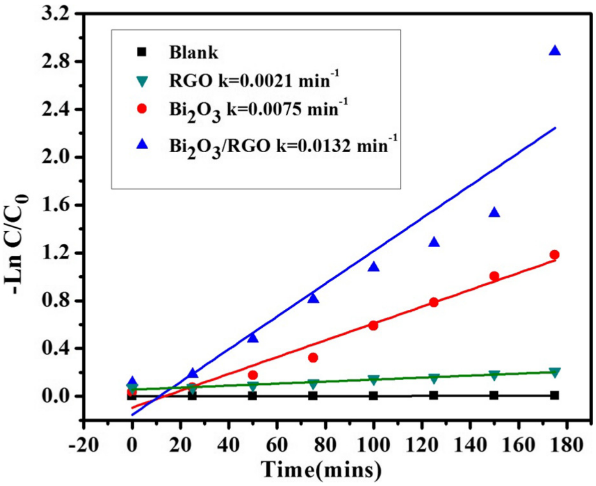

Fig. 16. Degradation rate constants of MB over the RGO, Bi_2O_3 and Bi_2O_3 rods/RGO composite.

composite is higher than those of the pure RGO and Bi_2O_3 samples. This increase in the degradation rate constant confirms the existence of a synergistic effect between RGO and Bi_2O_3 counterparts in the composite.

4. Conclusions

The Bi_2O_3 rods/RGO nanocomposite has been successfully synthesized by using simple precipitation and calcination method. As compared with the Bi_2O_3 electrode, Bi_2O_3 rods/RGO composite electrode exhibits higher capacitive performances due to the additional contribution from RGO. A maximum specific capacitance of 1041 F g^{-1} obtained at a current density of 2 A g^{-1} for the Bi_2O_3 rods/RGO composite as compared with 891 F g^{-1} for the pure Bi_2O_3. Therefore, this Bi_2O_3 rods/RGO composite is considered as a supercapacitor material. Furthermore the strong interfacial contact between the RGO sheets and Bi_2O_3 counterparts in the composite enhances the photocatalytic activity of Bi_2O_3 rods/RGO composite. Photocatalytic experiments showed that the Bi_2O_3 rods/RGO composite effectively degraded the MB dye (96%) under the visible light irradiation. Hence this Bi_2O_3 rods/RGO composite has potential to be applied in energy and environmental purposes.

Acknowledgment

The corresponding author would like to thank the Department of Science and Technology, (DST) India for providing the fund under "Early Career Research Award Scheme" (ECR/2016/001535/CS). Furthermore the authors acknowledge the UGC SERO-Hyderabad (MRP-5692/15(SERO/UGC)) for the financial support to carry out this research work.

Appendix A. Supplementary material

Supplementary data associated with this article can be found, in the online version, at http://dx.doi.org/10.1016/j.jcis.2017.03.086.

References

[1] K. Zhang, X. Han, Z. Hu, X. Zhang, Z. Tao, J. Chen, Chem. Soc. Rev. 44 (2015) 699–728.
[2] B. Wang, J.S. Chen, Z. Wang, S. Madhavi, X.W. Lou, Adv. Energy Mater. 2 (2012) 1188–1192.
[3] Y. Fan, H. Shao, J. Wang, L. Liu, J. Zhang, C. Cao, Chem. Commun. 47 (2011) 3469–3471.
[4] P. Zhang, Y. Yang, Z. Ma, Y. Wang, Y. Pan, C. Lu, Mater. Lett. 164 (2016) 421–424.
[5] H. Chen, J. Jiang, L. Zhang, T. Qi, D. Xia, H. Wan, J. Power Sources 248 (2014) 28–36.
[6] F.Z. Amir, V.H. Pham, D.W. Mullinax, J.H. Dickerson, Carbon 107 (2016) 338–343.
[7] E.C. Vermisoglou, E. Devlin, T. Giannakopoulou, G. Romanos, N. Boukos, V. Psycharis, C. Lei, C. Lekakou, D. Petridis, C. Trapalis, J. Alloys Compd. 590 (2014) 102–109.
[8] X. Lu, D. Zheng, T. Zhai, Z. Liu, Y. Huang, S. Xie, Y. Tong, Energy Environ. Sci. 4 (2011) 2915–2921.
[9] X. Huang, W. Zhang, Y. Tan, J. Wu, Y. Gao, B. Tang, Ceram. Int. 42 (2016) 2099–2105.
[10] H. Wang, D. Liu, X. Duan, P. Du, J. Guo, P. Liu, Mater. Design 108 (2016) 801–806.
[11] R.B. Ambade, S.B. Ambade, N.K. Shrestha, Y.C. Nah, S.H. Han, W. Lee, S.H. Lee, Chem. Commun. 49 (2013) 2308–2310.
[12] S. Vijayakumar, S. Nagamuthu, G. Muralidharan, ACS Appl. Mater. Interfaces 5 (2013) 2188–2196.
[13] H.T. Zhang, X. Zhang, D.C. Zhang, X.Z. Sun, H. Lin, C.H. Wang, Y.W. Ma, J. Phys. Chem. B 117 (2013) 1616–1627.
[14] J. Zhang, Y. Yu, L. Liu, Y. Wu, Nanoscale 5 (2013) 3052–3057.
[15] X. Lu, H. Dou, S. Yang, L. Hao, L. Zhang, L. Shen, F. Zhang, X. Zhang, Electrochim. Acta 56 (2011) 9224–9232.
[16] K. Li, B. Chai, T. Peng, J. Mao, L. Zan, ACS Catal. 3 (2013) 170–177.
[17] J. Zhang, J. Yu, Y. Zhang, Q. Li, J.R. Gong, Nano Lett. 11 (2011) 4774–4779.
[18] R. Daghrir, P. Drogui, D. Robert, J. Photochem. Photobiol., A 238 (2012) 41–52.
[19] Y. Zhu, Y. Wang, Q. Ling, Y. Zhu, Appl. Catal. B: Environ. 200 (2017) 222–229.
[20] W. Zhao, Y. Liu, Z. Wei, S. Yang, H. He, C. Shen, Appl. Catal. B: Environ. 185 (2016) 242–252.
[21] L. Guishi, C. Lijun, Z. Bing, L. Yi, Mater. Lett. 168 (2016) 143–145.
[22] J. Rong, T. Zhang, F. Qiu, X. Rong, X. Zhu, X. Zhang, J. Alloys Compd. 685 (2016) 812–819.
[23] M.D. Han, T. Sun, P.Y. Tan, X.F. Chen, O.K. Tan, M.S. Tse, RSC Adv. 3 (2013) 24964–24970.
[24] Y. Yan, Z. Zhou, Y. Cheng, L. Qiu, C. Gao, J. Zhou, J. Alloys Compd. 605 (2014) 102–108.
[25] R. Li, D. Wang, L. Ge, S. He, H. Chen, L. Guo, Ceram. Int. 40 (2014) 2599–2603.
[26] X. Guo, X. Li, C. Lai, W. Li, D. Zhang, Z. Xiong, Appl. Surf. Sci. 331 (2015) 455–462.
[27] J. Li, Q. Wu, G. Zan, Eur. J. Inorg. Chem 35 (2015) 5751–5756.
[28] A. Hameed, T. Montini, V. Gombac, P. Fornasiero, J. Am. Chem. Soc. 130 (2008) 9658–9659.
[29] A. Hameed, M. Aslam, I.M.I. Ismail, Salah, P. Fornasiero, Appl. Catal. B – Environ. 163 (2015) 444–451.
[30] F.L. Zheng, G.R. Li, Y.N. Ou, Z.L. Wang, C.Y. Su, Y.X. Tong, Chem. Commun. 46 (2010) 5021–5023.
[31] T.P. Gujar, V.R. Shinde, C.D. Lokhande, S.H. Han, J. Power Sources 161 (2006) 1479–1485.
[32] D. Yuan, J. Zeng, N. Kristian, Y. Wang, X. Wang, Electrochem. Commun. 11 (2009) 313–317.
[33] X. Huang, W. Zhang, Y. Tan, J. Wu, Y. Gao, B. Tang, Ceram. Int. 42 (2016) 2099–2105.
[34] S.X. Wang, C.C. Jin, W.J. Qian, J. Alloys Compd. 615 (2014) 12–17.
[35] K.S. Novoselov, V.I. Fal'ko, L. Colombo, P.R. Gellert, M.G. Schwab, K. Kim, Nature 490 (2012) 192–200.
[36] Y. Shao, H. Wang, Q. Zhang, Y. Li, J. Mater. Chem. C 1 (2013) 1245–1251.
[37] E. Paek, A.J. Park, K.E. Kweon, G.S. Hwang, J. Phys. Chem. C 117 (2013) 5610–5616.

[38] S. Vadivel, A.N. Naveen, V.P. Kamalakannan, P. Cao, N. Balasubramanian, Appl. Surf. Sci. 351 (2015) 635–645.
[39] L. Leontie, M. Caramana, G.I. Rusu, J. Optoelectron. Adv. Mater. 2 (2000) 385–389.
[40] S. Vadivel, V.P. Kamalakannan, Keerthi, N. Balasubramanian, Ceram. Int. 40 (2014) 14051–14060.
[41] A. Qian, K. Zhuo, B.N. Choi, S.J. Lee, J.W. Bae, P.J. Yoo, C.H. Chung, J. Alloys Compd. 688 (2016) 814–821.
[42] M. Chakrabarthi, S. Dutta, S. Chattapadhyay, A. Sarkar, D. Sanyal, A. Chakrabarti, Nanotechnology 15 (2004) 1792–1796.
[43] A.A. Ensafi, N. Ahmadi, B. Rezaei, J. Alloys Compd. 652 (2015) 39–47.
[44] Y.C. Zhang, H. Yang, W.P. Wang, H.M. Zhang, R.S. Li, X.X. Wang, R.C. Yu, J. Alloys Compd. 684 (2016) 707–713.
[45] X. Zheng, H. Wang, C. Wang, Z. Deng, L. Chen, Y. Li, T. Hasan, B.L. Su, Nano Energy 22 (2016) 269–277.
[46] N. Duraisamy, A. Numan, S.O. Fatin, K. Ramesh, S. Ramesh, J. Colloid Interface Sci. 471 (2016) 136–144.
[47] A. Shanmugavani, R. Kalaiselvan, Electrochim. Acta 189 (2016) 283–294.
[48] A.N. Naveen, S. Selladurai, Electrochim. Acta 173 (2015) 290–301.
[49] A.N. Naveen, S. Selladurai, Mater. Sci. Semiconduct. Proc. 40 (2015) 468–478.
[50] U. Alver, A. Tanriverdi, Appl. Surf. Sci. 378 (2016) 368–374.
[51] X. Yan, X. Tong, J. Wang, C. Gong, M. Zhang, L. Liang, Mater. Lett. 95 (2013) 1–4.
[52] W. Zeng, G. Zhang, S. Hou, T. Wang, H. Duan, Electrochim. Acta 151 (2015) 510–516.
[53] Y. Tang, B. Cheng, Energy 112 (2016) 755–761.
[54] K. Mohanapriya, G. Ghosh, N. Jha, Electrochim. Acta 209 (2016) 719–729.
[55] S. Nagamuthu, S. Vijayakumar, G. Muralidharan, Dalton Trans. 43 (2014) 17528–17538.
[56] K. Xu, J. Chao, W. Li, Q. Liu, Z. Wang, X. Liu, R. Zou, J. Hu, RSC Adv. 4 (2014). 34307–32314.
[57] S. Vijayakumar, S. Nagamuthu, G. Muralidharan, ACS Sustain. Chem. Eng. 1 (2013) 1110–1118.
[58] L. Cheng, Y. Kang, Catal. Commun. 72 (2015) 16–19.
[59] N. Mohaghegh, E. Rahimi, Solid State Sci. 56 (2016) 10–15.
[60] P. Xiong, Q. Chen, M. He, X. Sun, X. Wang, J. Mater. Chem. 22 (2012) 17485–17493.
[61] F. Wang, Y. Wang, X. Zhan, M. Safdar, J. Gong, J. He, Cryst. Eng. Commun. 16 (2014) 1389–1394.
[62] D. Maruthamani, D. Divakar, M. Kumaravel, J. Ind. Eng. Chem. 30 (2015) 33–43.
[63] Z. Bin, L. Hui, Appl. Surf. Sci. 357 (2015) 439–444.
[64] X. Gong, W.T. Teoh, J. Catal. 332 (2015) 101–111.
[65] S.T. Senthilkumar, R. Kalaiselvan, M. Ulaganthan, J.S. Melo, Electrochim. Acta 115 (2014) 518–524.
[66] J. Ma, S. Zhu, Q. Shan, S. Liu, Y. Zhang, F. Dong, H. Liu, Electrochim. Acta (168) 97–103.